

Research Article

Synthesis of MnO₂ Hollow Nanospheres through Selective Etching Method as an Effective Absorbent to Remove Methyl Orange from Aqueous Solution

Xiaohui Hu,^{1,2,3} Fangsong Zhang ^{1,2,3} Hong Wang,^{1,2,3} Xinyi Zhang,^{1,2,3}
and Linfeng Zhang ^{1,2,3,4}

¹Key Laboratory for Green Chemical Process of Ministry of Education, Wuhan Institute of Technology, Wuhan 430205, China

²Key Laboratory of Novel Reactor and Green Chemical Technology of Hubei Province, Wuhan Institute of Technology, Wuhan 430205, China

³School of Chemical Engineering and Pharmacy, Wuhan Institute of Technology, Wuhan 430205, China

⁴School of Chemical Engineering and Technology, Tianjin University, Tianjin 300072, China

Correspondence should be addressed to Linfeng Zhang; lfzhang@wit.edu.cn

Xiaohui Hu and Fangsong Zhang contributed equally to this work.

Received 14 May 2019; Revised 9 September 2019; Accepted 16 September 2019; Published 6 November 2019

Guest Editor: Ziyu Zhou

Copyright © 2019 Xiaohui Hu et al. This is an open access article distributed under the Creative Commons Attribution License, which permits unrestricted use, distribution, and reproduction in any medium, provided the original work is properly cited.

The discharge of dye wastewater has become an unavoidable problem for human health and the environment. Developing an economical and rapid method to prepare effective adsorbents for selective removal of dyes is extremely urgent. In this work, MnO₂ hollow nanospheres (MHNSs) were prepared through the selective etching method with the MnCO₃ as the sacrificial template. The effect of the pH value, contact time, and initial concentration on the adsorption of methyl orange (MO) onto the MHNSs was systematically investigated. The unique mesoporous hollow structure and large BET surface area (43.74 m²/g) of MHNSs lead to an excellent adsorption capacity (1677.14 mg/g) at the optimal condition. Furthermore, the prepared MHNSs also showed great stability (90% removal rate after four cycles). The adsorption kinetics data fitted well with the pseudo-second-order kinetic model ($R^2 > 0.9997$). The overall process was jointly controlled by external mass transfer and intraparticle diffusion, and intraparticle diffusion was the dominant factor. The adsorption isotherm results showed that the Freundlich model was more accurate to describe the experimental data than the Langmuir model. The thermodynamic analysis showed that the adsorption of MO on MHNSs was spontaneous and exothermic. Moreover, the calculated ΔG° and the XPS spectra showed that the process was mainly a physical process. It is expected that MHNS has a potential application for purifying dye wastewater due to its great adsorption performance and excellent stability.

1. Introduction

Water pollution has become a worrying challenge for human health and the ecosystem [1–7]. The release of dye wastewater leads to serious environmental problems. However, the treatment of this class of wastewater has proven to be quite difficult because of its stable and complex aromatic structure [8–12]. Therefore, there is an urgent need to design an efficient method for removing dye molecules from wastewater. Various technologies such as photoelectrocatalysis, mem-

brane filtration, chemical oxidation, and adsorption have been proposed to solve this problem [13–18]. Nevertheless, these methods are often expensive, technically demanding, or only effective at a certain concentration. The adsorption technology has been considered to be an efficient, nontoxic, and economic water treatment technique, and the key of this technology is to develop highly effective adsorbents.

Currently, as one of typical metal oxides, manganese oxide with various structures and morphologies was widely used in the fields of catalysis, electrochemical supercapacitors,

and adsorption. The morphology and structure of prepared manganese oxide are seriously restricted by its synthetic route and conditions. Many researchers have prepared manganese oxide composite adsorbents with uniform microstructure and highly specific surface area through molten salt, sol-gel, coprecipitation, and hydrothermal processes [19–23]. Among reported materials, the hollow micro-/nanostructures are a special class of materials due to their unique morphologies, which have superior advantages such as high BET surface area, surface permeability, and potential scale-dependence [24–27]. Gheju et al. have reported an efficient MnO_2 adsorbent for adsorption of Cr^{6+} and investigated the influence of the pH value, temperature, and initial Cr^{6+} concentration [28]. The highest adsorption capacity was obtained at 20°C and pH 5.9. Li. et al. have successfully synthesized hierarchical hollow MnO_2 microspheres by a hydrothermal method, and the prepared materials show high performance for the adsorption of benzene [29]. However, conventional MnO_2 -based adsorbents were usually irregular nanoparticles or required a high temperature/pressure condition. Therefore, it is necessary to design a simple operation and short-reaction-time method for preparing a MnO_2 adsorbent with high efficiency.

In this study, hollow manganese dioxide adsorbents with high efficiency were prepared by a low-temperature acid etching method [30]. The size and shell thickness of the hollow manganese oxide could be exactly controlled by adjusting the amount of etch acid and reaction time. Subsequently, the adsorption capacity of prepared hollow manganese oxide microspheres under different pHs, temperatures, and initial concentrations was evaluated by the adsorption of MO. The adsorption kinetics, rate-determining step, and thermodynamic analysis of the adsorption process were also investigated. Moreover, the possible mechanism of a MO molecule absorbed onto the MHNSs was studied and discussed.

2. Experimental

2.1. Materials. Methyl orange, sodium hydroxide, hydrochloric acid, potassium permanganate, manganese nitrate, ammonium carbonate, and polyethylene glycol were all purchased from Sinopharm Chemical Reagent Co. Ltd.

2.2. Synthesis of the MHNSs. Typically, 1.6 g $\text{Mn}(\text{NO}_3)_2$ (50% solution) and 0.5 g PEG powder were dissolved in 100 mL of ethanol-water solution ($v : v = 1 : 1$) under 40°C water bath. Afterward, 1.6 g $(\text{NH}_4)_2\text{CO}_3$ powder was dissolved into 20 mL deionized water and then transferred to a 20 mL syringe. The above $(\text{NH}_4)_2\text{CO}_3$ solution was slowly dripped into the manganese nitrate solution, and the entire drip process was completed within 2 h. After aging for 4 h, the product was collected, washed, and fully dried at 60°C. Then, 0.5 g of prepared MnCO_3 powder was dispersed in 20 mL of distilled water and 25 mL of 0.03 M KMnO_4 solution was added into the suspension. Then, 8 mL 2.5 M hydrochloric acid solution was added into the mixture with fierce stirring. The etching reaction was sustained for 2 min, then the product was filtered immediately and washed with distilled water. Finally, the obtained solid was dried in a vacuum oven at 60°C for 12 h.

2.3. Characterization of the Samples. The crystal structure of the prepared MnCO_3 template and MHNSs was studied with X-ray powder diffraction (XRD, Bruker D8 Advance, $\text{Cu K}\alpha$, $\lambda = 0.15418$ nm). The morphology of the samples was characterized by field emission scanning electron microscopy (FESEM, ZEISS Merlin compact) and transmission electron microscopy (TEM, TecnaiG2 F20 S-TWIN). The surface functional groups were analyzed by Fourier transform infrared (FT-IR) spectra (Nicolet 5700). The BET surface area, pore volume, and pore size distribution of the MHNSs characterized at 77 K were investigated using an Autosorb-iQ Quantachrome surface area and porosity analyzer. The surface compositions were analyzed by X-ray photoelectron spectroscopy (XPS, ESCALab 250Xi).

2.4. Evaluation of the Adsorption Capacity. The MO solution was used as a model pollutant to evaluate the adsorption performance of the as-prepared MHNSs. In order to study the effect of initial concentrations, the MO solution with selected concentrations (50, 100, 150, 200, 250, and 300 mg L^{-1}) was prepared. Similarly, the pH value of the solution was adjusted from 2.0 to 11.0 using 1 M HCl or NaOH to investigate the effect of pH value. The 20 mg MHNS adsorbent was added into 200 mL MO solution, and the solution was kept at 15°C under stirring at 300 rpm. At selected intervals, about 3 mL suspension was collected and filtered to remove the catalysts using a 0.45 μm membrane filtration. The MO concentration was recorded on a Lambda 35 UV-Vis spectrometer. The equilibrium absorption capacity of the MHNSs q_e (mg g^{-1}) was calculated using the following equation [31, 32]:

$$q_e = \frac{V(C_0 - C_e)}{m}, \quad (1)$$

where C_0 (mg/L) is the initial MO concentration, C_e (mg/L) is the equilibrium MO concentration, V (L) is the volume of the solution, and m (g) is the mass of the added MHNS adsorbents.

The reusability of the MHNSs was a very important factor for industrial application. In the stability evaluation, the used adsorbent was collected. Then, the stability test of the MHNSs was conducted by repeating the MO solution under the same conditions for five cycles without any regeneration treatment [33, 34].

3. Results and Discussion

3.1. XRD, Morphology, and the BET Measurements of the MHNSs. In this study, low-cost $(\text{NH}_4)_2\text{CO}_3$ and KMnO_4 were selected as the raw materials. The MHNSs were successfully fabricated by the selective etching method with the MnCO_3 as the template. The typical SEM and TEM images of the MnCO_3 template and MHNSs are shown in Figure 1. The MnCO_3 templates show a well-defined microsphere structure with a diameter of about 2 μm , and the microspheres show a slight agglomeration between each other. Furthermore, some broken microspheres demonstrated that the spherical hollow structure of prepared MHNSs is derived from the selective etching of the MnCO_3 template. The

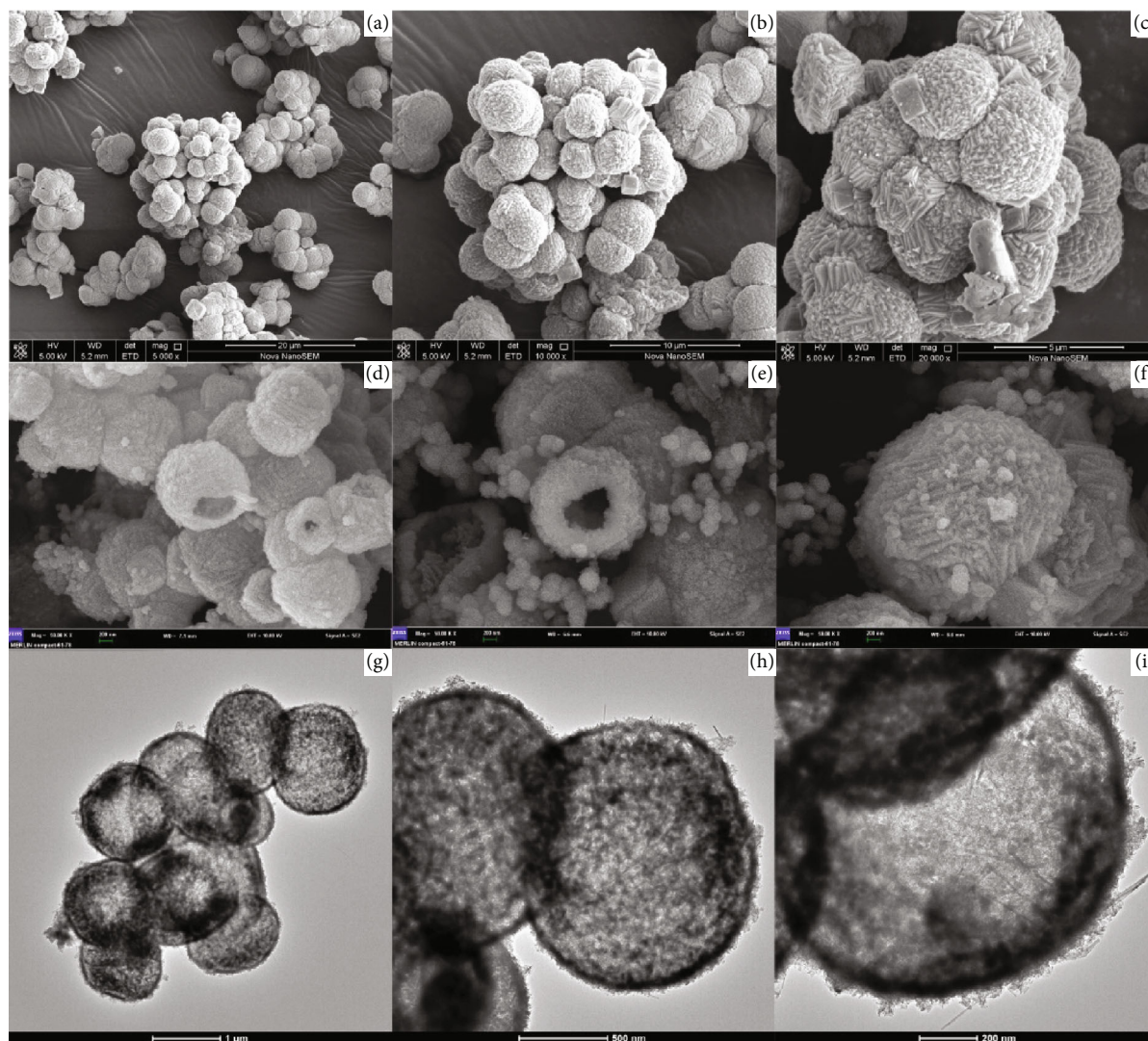
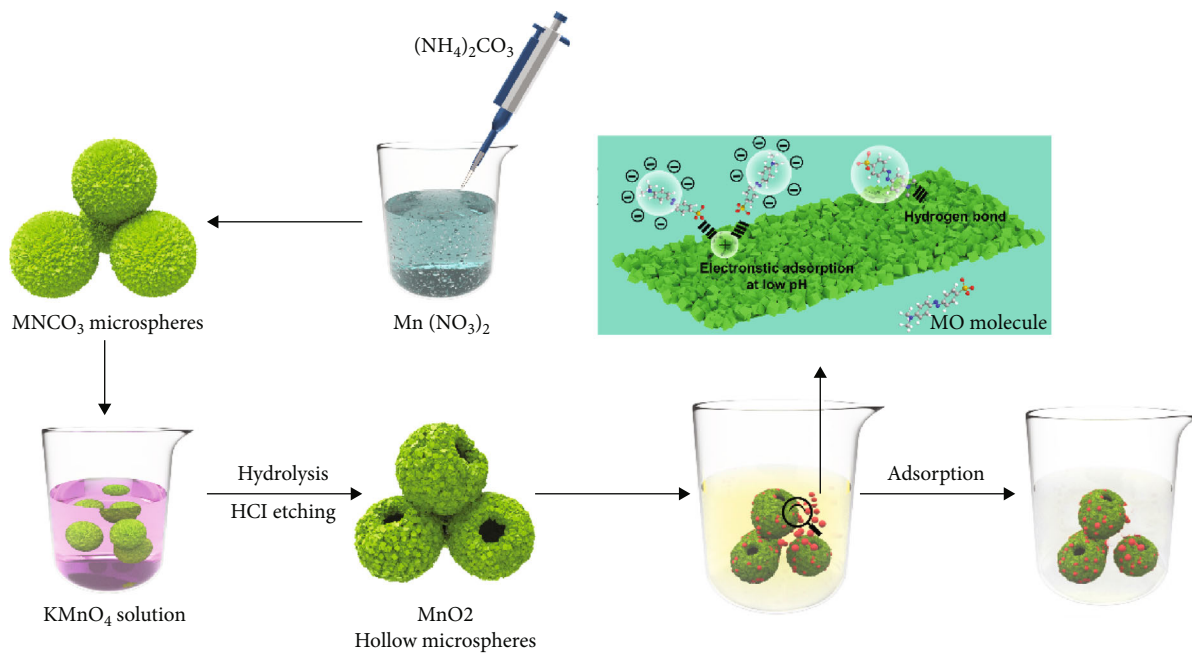


FIGURE 1: Scheme illustration and the typical SEM and TEM images of the samples.

thickness of the spherical shell was about 300 nm. As shown in the high-resolution images, the original smooth nano-sheets were replaced by the rough MnO_2 nanoparticles. When the KMnO_4 solution was added, the MnO_2 nanoparticles formed by hydrolysis were adhered on the surface of the MnCO_3 template. At the same time, the MnCO_3 template was selectively etched by the HCl solution, then the MHNSs with a spherical hollow structure were obtained. Meanwhile, it can be observed that some dispersed MnO_2 microsphere with the diameter at 200–300 nm coated on the surface of the hollow spheres. Furthermore, the hollow structure of prepared MHNSs was confirmed by the TEM techniques (Figure 1(g)–1(i)). The diameter of the hollow shells range from 1 μm to 2 μm , and the shell thickness was about 300 nm, which was consistent with the SEM analysis. Thus, a plausible formation mechanism was proposed in the scheme illustration figure (as shown in Figure 1).

Figure 2 showed the XRD patterns of prepared MnCO_3 and MHNS samples. The diffraction peaks at $2\theta = 24.25^\circ$, 31.36° , and 51.68° can be assigned to the (012), (104), and (116) planes of MnCO_3 (JCPDS card no. 44-1472), respectively. For the MHNS sample, the diffraction peaks at $2\theta = 37.12^\circ$, 45.01° , and 65.70° correspond to the (311), (400) and (440) crystal planes, respectively, which was consistent with the $\alpha\text{-MnO}_2$ (JCPDS card no. 44-0992). However, it can be observed that the MHNSs exhibit low and broad diffraction peaks. As mentioned in the FESEM discussions, the KMnO_4 will hydrolyze to form MnO_2 nanoparticles coated on the surface of the MnCO_3 template. Meanwhile, the MnO_2 maintains a low level of crystallinity due to the low-temperature and short-time reaction conditions. Thus, the characteristic peak intensity of the MHNSs was weak compared to that of prepared MnCO_3 templates.

In order to investigate the specific surface area, pore size distribution and pore volume of the MHNSs, the N_2 adsorption-desorption isotherm was conducted and the result was as shown in Figure 3. The N_2 adsorption-desorption isotherms exhibit type-IV isotherms. The BET surface area, total pore volume, and average pore size are determined to be $43.74 \text{ m}^2 \text{ g}^{-1}$, $0.1133 \text{ cm}^3 \text{ g}^{-1}$, and 1.04 nm, respectively. Thus, it can be concluded that the prepared MHNS sample is dominated by mesopores, promoting the adsorption ability for the MO molecule.

3.2. Effect of pH Value on MO Adsorption. Many studies have reported that the adsorption capacity of the adsorbent was pH-dependent. The reason can be that the pH value can influence the surface charge of the adsorbent and the degree of ionization/dissociation of the MO molecules. Thus, the adsorption on MO at different pH values are performed and shown in Figure 4. With the increase of pH value from 2.0 to 11.0, the adsorption capacity of MHNSs on MO decreases from 99% to 2%. Obviously, MHNSs can only effectively adsorb MO molecules under acidic conditions, but it could hardly act at alkaline or neutral solution conditions. Since most of the free hydroxyl groups on the surface of MHNSs are derived from the hydrogen ions in the solution, the surface is positively charged. However, the sulfonate ions ionized by methyl orange molecules are negatively

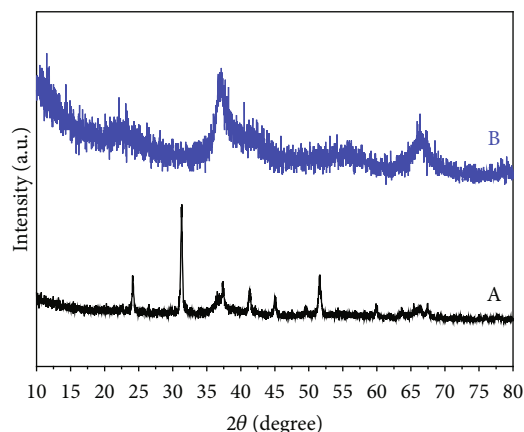


FIGURE 2: XRD patterns of the MnCO_3 template (A) and the MHNS samples (B).

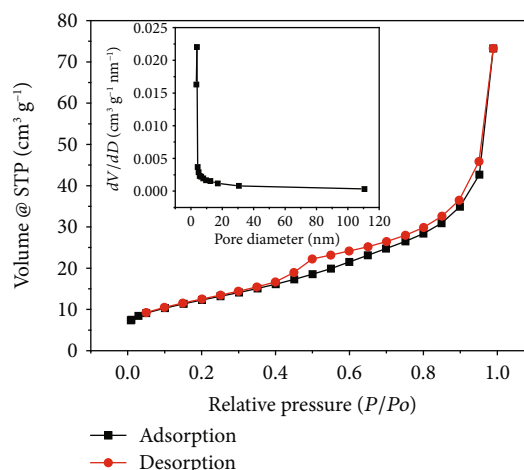


FIGURE 3: N_2 adsorption-desorption isotherm (inset: the pore size distribution).

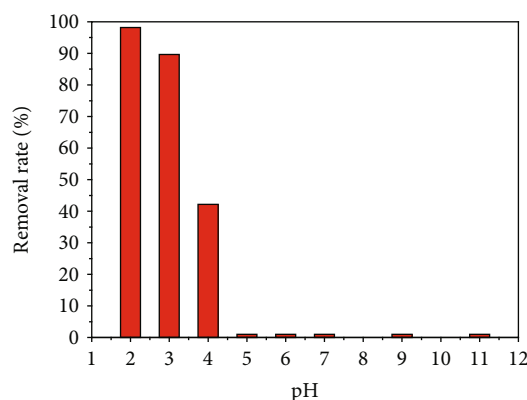


FIGURE 4: Effect of solution pH on the MO adsorption (experimental conditions: initial dye concentration: 50 mg L^{-1} , adsorbent dosage: 20 mg/200 mL, temperature: 288 K, and contact time: 120 min).

charged under acidic condition. Therefore, the negatively charged sulfonate ions will be adhered to the positively charged MHNS surface, then forming the ligand complex.

At an acidic pH value, the solution is rich of hydrated hydrogen ions (H^+ and H_3O^+), and the surface of MHNSs become more positively charged, which makes it more likely to adsorb MO in solution. On the contrary, the adsorption efficiency is relatively low under alkaline conditions. Moreover, there is a competitive adsorption relationship between the negatively charged MO ions and excessive hydroxide ions. With the increase of pH value, the concentration of hydroxide ions in the solution increases and the negative charge on the surface of MHNSs increases. So the Coulombic repulsion between the hydroxide ions and the anionic dye was enhanced, and the adsorption activity of MHNSs on the MO solution was decreased. Therefore, the significant influence of the adsorption amount of the MHNS surface was caused by the pH value of the solution, indicating that the electrostatic interaction may be the main mechanism for the adsorption process of anionic dyes. It can also be seen from Figure 5 that the adsorption process of MHNSs on MO is very fast, in which almost 90% of MO molecules were removed within 5 min.

3.3. Effect of Contact Time and Initial Concentration. Three initial concentrations (50, 100, and 150 $mg L^{-1}$) of MO solutions were chosen to investigate the equilibrium time and the adsorption capacity of prepared MHNSs and the results was shown as in the Figure 6. With the increase of the initial concentration, the equilibrium adsorption capacity (q_e) of the MHNSs increased from 475.95 $mg g^{-1}$ to 1420.08 $mg g^{-1}$, indicating that the initial concentration had a significant impact on the adsorption capacity. The reason can be ascribed to the increasing driving force of concentration gradient. Moreover, the adsorption rate of MO was rapid at the initial 30 min and then slows (at the contact time of 30~120 min). During the initial stage, the MO molecules were rapidly absorbed by the MHNS adsorbent due to the sufficient adsorption sites on the surface. Then, the adsorption rate slowed down with the dwindling number of active sites and the increasing mutual repulsive forces between the MO molecules on the surface of MHNSs and the bulk solution. The reusability of the MHNS adsorbent was tested with the initial concentration of MO solution at 50 $mg L^{-1}$, and the results are shown in Figure 7. It was found that the removal rate of MO was still maintained at 90% after four cycles. Therefore, it can be concluded that the MHNS adsorbent exhibited well adsorption stability on the MO solution.

3.4. Evaluation of Adsorption Kinetics. The Lagergren-first-order equation, pseudo-second-order equation, and intra-particle diffusion model were used to investigate the adsorption kinetics of the MO molecule on MHNSs, and the correlation coefficient value (R^2) was used to select the best-fit model [35, 36]. Figures 8–10 present the analysis results of MHNSs acted on the MO solution with different dynamic models. The pseudo-first-order kinetic model was specified as follows [37, 38]:

$$\ln(q_e - q_t) = \ln(q_e) - k_1 t, \quad (2)$$

where q_t (mg/g) is the adsorption capacity at time t (min),

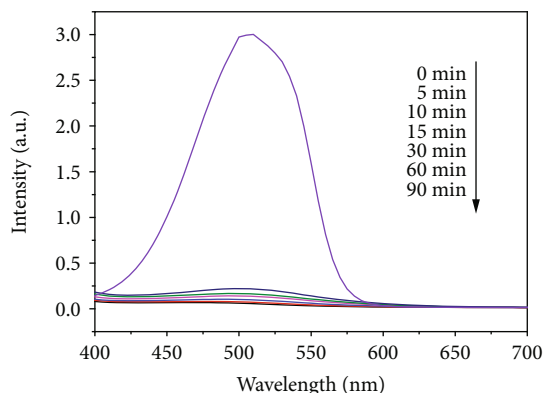


FIGURE 5: Time-dependent absorbance spectra of the adsorption process at selected intervals.

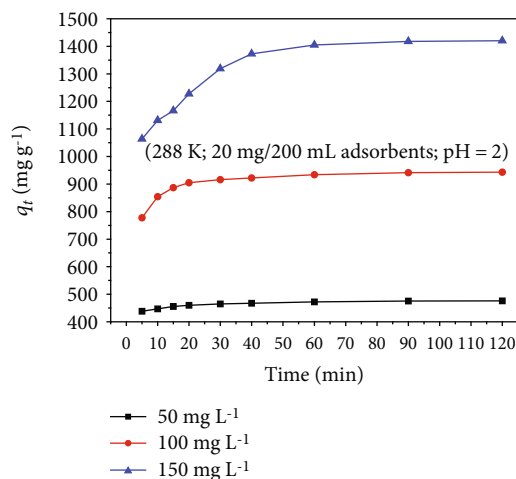


FIGURE 6: Effect of contact time on MO adsorption at different initial concentrations.

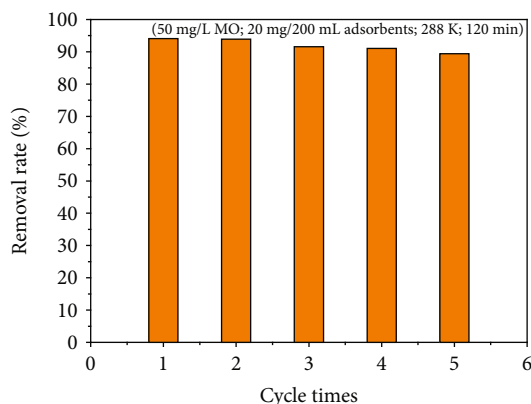


FIGURE 7: Efficiency of the MHNS composite after five cycles.

q_e (mg/g) is the equilibrated adsorption capacity, and k_1 (min^{-1}) is the rate constant of the pseudo-first-order kinetic model.

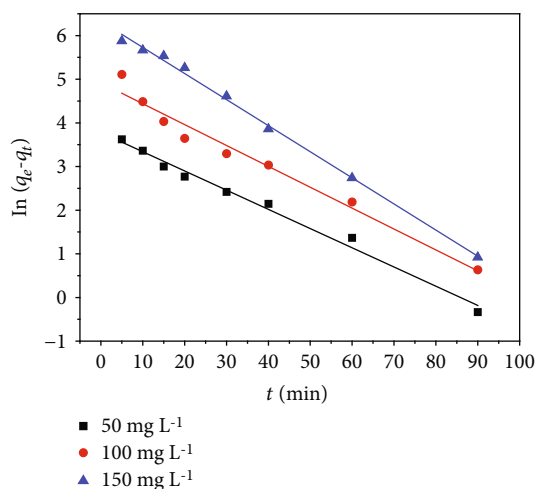


FIGURE 8: Regressions of kinetic plots at different initial concentrations: pseudo-first-order kinetic model.

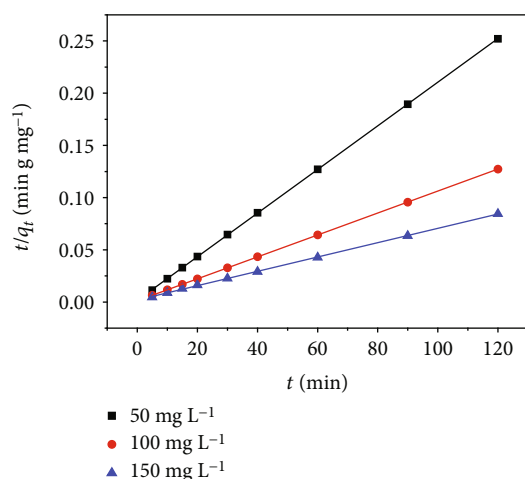


FIGURE 9: Regressions of kinetic plots at different initial concentrations: pseudo-second-order kinetic model.

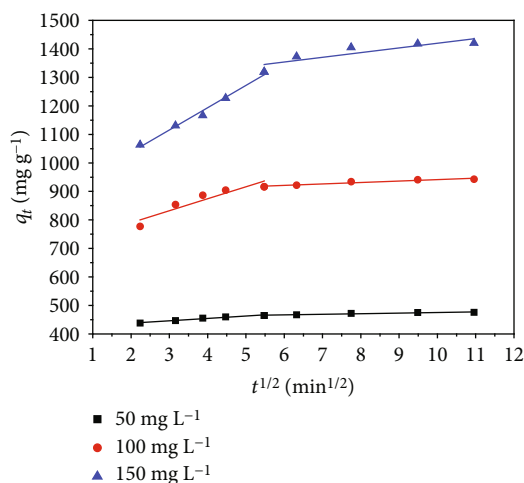


FIGURE 10: Regressions of kinetic plots at different initial concentrations: intraparticle mass transfer diffusion model.

The value of k_1 can be calculated from the plots of $\ln(q_e - q_t)$ versus t according to the equation. The linear formula of the pseudo-second-order kinetic model can be expressed as follows [39, 40]:

$$\frac{t}{q_t} = \frac{1}{k_2 q_e^2} + \frac{t}{q_e}, \quad (3)$$

where k_2 ($\text{g mg}^{-1} \text{min}^{-1}$) is the rate constant of the pseudo-second-order kinetic model.

The slope and intercept of the linear plots of t/q_t against t was used to calculate the value of k_2 and q_e according to the equation.

Then, the initial adsorption rate h ($\text{mg g}^{-1} \text{min}^{-1}$) was determined as follows [41]:

$$h = k_2 q_e^2. \quad (4)$$

The actual rate-controlling step of the MO adsorbed on the MHNSs was very crucial for researching the adsorption mechanism. However, the aforementioned two kinetic models could not predict it exactly, then the intraparticle mass transfer diffusion model proposed by Weber-Morris was employed. And the calculation equation was as follows [42, 43]:

$$q_t = k_i t^{1/2} + C, \quad (5)$$

where k_i ($\text{mg g}^{-1} \text{min}^{-1/2}$) is the intraparticle diffusion rate constant and C is the constant that reflects the thickness of the boundary layer.

The graph of q_t against the square root of time can be used to calculate the value of k_i and the constant C .

The three kinetic model parameters of MO adsorption onto MHNSs with different initial concentrations are shown in Table 1. It could be observed that all the experimental data agreed well with the pseudo-second-order kinetic model ($R^2 > 0.9997$). Therefore, the pseudo-second-order kinetic model was selected to analyze the adsorption process of MO molecule onto MHNSs in this study.

Generally, the adsorption process of MO on the MHNSs was controlled by the following three steps: external mass diffusion, intraparticle diffusion, and the adsorption on the MHNS surface. Because the adsorption process was very fast, this rate-limiting step often was not considered in this study. In order to determine the exact rate-controlling step, the intraparticle diffusion model was involved in the analysis process for MO adsorption on the MHNSs, and the results are shown in Figure 10.

Multivariate linear regression was used to analyze the MHNS adsorption MO data. According to the intraparticle diffusion model, the linear plot of adsorption capacity versus square root of time ($t^{1/2}$) indicated that there were two obvious regions in the graph. The first region was from 0 to 30 minutes, and the second one was 30-120 minutes. The linear portion in the first region has a larger slope, which represents the external mass transfer process. However, during the second stage, the adsorption capacity of MHNSs on MO still

TABLE 1: Parameters of pseudo-first- and pseudo-second-order adsorption kinetic models and the intraparticle diffusion model at various concentrations.

C_0 (mg L ⁻¹)	$q_{e,exp}$	Pseudo-first-order model					
		k_1	q_e	r^2			
50	475.95	0.04402	43.793	0.9869			
100	942.99	0.04788	136.904	0.9683			
150	1420.08	0.0598	560.220	0.9962			
C_0 (mg L ⁻¹)	Pseudo-second-order model			Intraparticle diffusion model			
	$k_2 \times 10^{-3}$	q_e	r^2	h	k_i	C	r^2
50	2.7822	478.469	0.9999	636.943	8.339	421.176	0.9562
100	0.9187	952.381	0.9999	833.333	42.114	705.854	0.8299
150	0.2349	1458.99	0.9997	500.000	78.136	881.039	0.9830

increased with $t^{1/2}$, but compared with the first stage, the slope of the linear portion was much smaller. This can be ascribed to the second stage which was controlled by the intraparticle diffusion. Additionally, all the linear portions did not pass through the origin, indicating that the intraparticle diffusion was not the only rate-controlling step in the MHNS adsorption process. The ratio of the diffusion duration of the external mass to the intraparticle is about 1 : 3, which means that the whole adsorption process was controlled by the external mass transfer and the intraparticle diffusion, and the intraparticle diffusion was superior to the external mass transfer.

3.5. Adsorption Isotherm Study. In order to further study the adsorption interaction between the MO and the MHNSs, the equilibrium adsorption data were analyzed and fitted using the Langmuir and Freundlich isothermal models in this study [44, 45]. The Langmuir isotherm can be expressed as follows:

$$\frac{C_e}{Q_e} = \frac{1}{Q_m K_L} + \frac{1}{Q_m} C_e, \quad (6)$$

where C_e (mg/L) is the equilibrium concentration, Q_e (mg/g) is the adsorption capacity of adsorbate per unit mass, Q_m is the Langmuir constant, and K_L is the adsorption rate.

The essential characteristic of the Langmuir equation was expressed by the dimensionless separation factor R_L :

$$R_L = \frac{1}{1 + K_L C_0}, \quad (7)$$

where K_L (L/mg) is the Langmuir isotherm constant, C_0 (mg/L) is the initial MO concentration, and R_L is the type of isotherm.

The linear form of the Freundlich equation is

$$\ln Q_e = \ln K_F + \frac{1}{n} \ln C_e, \quad (8)$$

where K_F (L/mg) is the adsorption capacity, and n is the definition of how favorable the adsorption process is.

As shown in Table 2, the R_L value of the Langmuir model was between 0 and 1 and the n value of the Freundlich model was between 1 and 10. These results indicated that the adsorption process of MO molecules on the MHNSs was favorable. In addition, the correlation coefficient results of different models showed that the Freundlich model had a better fit of experimental data than that of the Langmuir model. When the temperature of the adsorption process increased from 273 K to 303 K, the maximum adsorption capacity of MO molecules on MHNSs decreased significantly from 1677.14 mg/g to 1589.40 mg/g. The maximum adsorption capacity of MHNSs and other adsorbents reported in literature on MO solution are listed in Table 3. It can be seen from the table that the saturated adsorption capacity of MHNSs was much higher than that of other adsorbents. Therefore, it can be considered that the prepared MHNSs have a potential application in the sewage treatment field.

3.6. Thermomechanical Analysis. In general, depth information such as the internal energy transformation can be analyzed by the thermodynamic parameters in the adsorption process. The standard Gibbs free energy change ΔG° , the standard molar enthalpy change ΔH° and the standard molar entropy change ΔS° were determined according to the adsorption thermodynamic equilibrium constants at different temperatures. For the adsorption process, the adsorption equilibrium constant K_0 can be defined by the following formula [55, 56]:

$$K = \frac{\alpha_s}{\alpha_e} = \left(\frac{\gamma_s}{\gamma_e} \right) \cdot \left(\frac{q_e}{C_e} \right), \quad (9)$$

where α_s is the activity (effective concentration) of adsorbed methyl orange and α_e is the activity of methyl orange in the equilibrium solution. γ_s is the activity coefficient of adsorption methyl orange. γ_e is the activity coefficient of methyl orange in equilibrium solution. With the progress of adsorption, the concentration of methyl orange in the solution keeps decreasing and tends to zero when the adsorption equilibrium is reached. Therefore, the equilibrium constant

TABLE 2: Parameters of the adsorption isotherm for the removal of MO by the MHNSs at different temperatures.

T (K)	q_m (mg g ⁻¹)	Langmuir			Freundlich		
		b	r^2	R_L	n	K_F	r^2
273	1718.712	0.2824	0.9992	0.01167~0.06614	1.6213	380.8478	0.9257
288	1688.416	0.2278	0.9989	0.01442~0.08071	1.1274	214.6052	0.9786
303	1633.290	0.2089	0.9981	0.01571~0.08737	1.1029	191.8282	0.9899

TABLE 3: Comparison of the adsorption capacities of MO onto various adsorbents.

Adsorbates	Adsorbents	q_{max} (mg g ⁻¹)	Reference
MO	Amine modified PIM-1 ultrafine fibers	312.50 mg g ⁻¹	[46]
	3-dimensional (3D) flower-like Ni/Al@PAB LDH	412.80 mg g ⁻¹	[47]
	Date palm ash (DPA) and MgAl-LDH composites	242.98 mg g ⁻¹	[48]
	Magnetic lignin-based carbon nanoparticles (MLBCN)	113.00 mg g ⁻¹	[49]
	Chitosan-lysozyme biocomposite (CLC)	435.00 mg g ⁻¹	[50]
	MnO ₂ -graphene-carbon nanotube (MnO ₂ -G-CNT)	476.19 mg g ⁻¹	[51]
	CaFe ₂ O ₄ and ZrO ₂ magnetic nanocomposite (CaF-ZO-MNC)	370.37 mg g ⁻¹	[52]
	An amorphous solid contains large cationic aMOC-1	359.00 mg g ⁻¹	[53]
	β -CD and PEI bifunctionalized magnetic (Fe ₃ O ₄ -PEI/ β -CD)	192.20 mg g ⁻¹	[54]
	The MnO ₂ hollow nanospheres (MHNSs)	1677.13 mg g ⁻¹	This work

K_0 value could be obtained by plotting $\ln(q_e/C_e)$ versus q_e and extrapolating q_e equal to zero.

For any interaction, the adsorption standard Gibbs free energy change ΔG° can be expressed by

$$\Delta G^\circ = -RT \ln(K_0), \quad (10)$$

$$\Delta G^\circ = \Delta H^\circ - T\Delta S^\circ.$$

From the above two formulas, K_0 can be concluded as follows:

$$\ln(K_0) = -\frac{\Delta H^\circ}{RT} + \frac{\Delta S^\circ}{R}, \quad (11)$$

where R is the standard gas constant (8.314 J mol⁻¹ K⁻¹) and T is the Kelvin temperature (K); ΔH° and ΔS° can be calculated from the slope and intercept of plot $\ln(K_0)$ versus $1/T$. The thermodynamic data is listed in Table 4. It can be seen that the ΔG° values at the three temperatures were all negative, indicating that the adsorption of MO on the surface of MHNSs was a spontaneous process and thermodynamically feasible. In general, the ΔG° of the physical adsorption process was less than that of the chemical adsorption process. Normally, the ΔG° value of the physical adsorption process was between -20 and 0 kJ mol⁻¹, while that of the chemisorption process was between -400 and -80 kJ mol⁻¹ [57]. And the adsorption standard value ΔH° of the physical process was 2~21 kJ mol⁻¹ [58]. Therefore, the value of ΔH° (-16.825) also suggested that the adsorption of MO onto the surface of MHNSs was mainly a physical process, which was also consistent with the previous results. Therefore, the adsorption process of MO on MHNSs was mainly a physical

TABLE 4: Values of thermodynamic parameters for the adsorption of the MO dye on the MHNSs.

T (K)	$\ln K_0$	ΔG° (kJ mol ⁻¹)	ΔH° (kJ mol ⁻¹)	ΔS° (J mol ⁻¹ K ⁻¹)
273	7.3756	-16.740		
288	6.7616	-16.189	-16.825	-1.160
303	6.6528	-16.759		

process. Moreover, the negative value of ΔH° revealed that the adsorption process is an exothermic process, which was well consistent with the aforementioned results that the adsorption capacity of MO decreased with the increase of temperature. Meanwhile, the negative ΔS° of the adsorption demonstrated that the MO molecule in bulk solution was in a more chaotic distribution compared to the ordered state (adsorbed on the surface of MHNSs).

3.7. Adsorption Mechanism Analysis. In order to further study the mechanism of the MO adsorption process on adsorbents, the FT-IR spectra of the fresh and used MHNS samples are shown in Figure 11. The weak peaks around at about 530 cm⁻¹ in the low frequency region could be attributed to the Mn-O and Mn-O-Mn shrink vibration [59, 60]. Importantly, the FT-IR spectra of the MHNS-MO sample were significantly different from its original spectrum. In the case of the MHNS-MO sample, the new peaks located at 1039, 1193, and 1384 cm⁻¹ correspond to the contraction vibrations of the -S=O, CH₃-, and CN bonds, respectively. And the peaks located at 818, 849 cm⁻¹ can be indexed to the fingerprint region indicating that MO molecules were concentrated on the surface of MHNSs [61, 62].

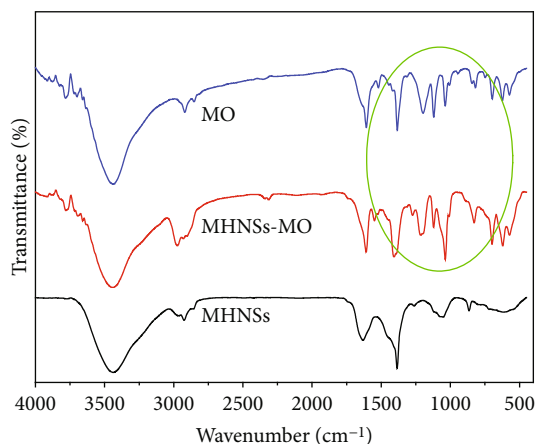


FIGURE 11: FT-IR spectra of pure MO and the MHNS composites before and after adsorption of MO.

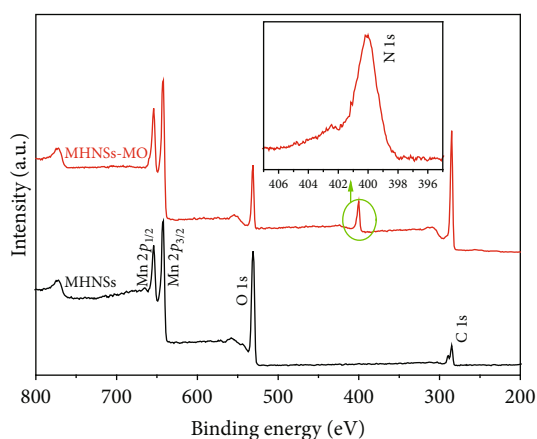


FIGURE 12: XPS spectra of the MHNS composites before and after adsorption of MO.

Generally, adsorption reaction may cause some changes of physical properties changes in the adsorbent, and the resulting change may help to investigate the adsorption reaction. As shown in Figure 12, the surface chemical composition and valence state of MHNSs before and after adsorption of MO molecules were characterized by XPS. It can be seen that the peaks of Mn $2p_{3/2}$ and Mn $2p_{1/2}$ were located at 642.1 eV and 653.5 eV, respectively, indicating that the Mn of the prepared MHNSs were in the form of Mn⁴⁺. The energy separation between the two peaks was 11.4 eV, which was well in agreement with the previous literatures [63, 64]. Furthermore, the position and intensity of the Mn $2p$ peaks did not change after the adsorption, which confirmed that the adsorption process of MO did not cause a significant change in the oxidation state of manganese. Additionally, it was found that there was a weak N 1s peak located at 399.8 eV for the adsorbed MHNS-MO spectrum, which indicated that a large amount of MO was adsorbed onto the MHNSs. These results indicated that the adsorption of MO molecules did not change the chemical composition and valence states of MHNSs. This adsorption process was

mainly a physical process, which was consistent with the conclusions in thermomechanical analysis.

4. Conclusions

The MnO₂ hollow nanospheres (MHNSs) were prepared through a selective etching method using MnCO₃ as sacrificial templates. The crystal structure, morphology, and BET surface area were investigated. The adsorption capacity of MO onto the MHNSs was systematically investigated by adjusting the pH value, the initial MO concentration, and the contact time. The prepared MHNSs showed an excellent adsorption capacity toward MO compared to other adsorbents. The adsorption kinetics followed the pseudo-second-order model. Moreover, the overall process was apparently controlled by the external mass transfer and intraparticle diffusion based on the adsorption kinetics data. The thermodynamic analysis showed that the adsorption of MO on MHNSs was a spontaneous, exothermic, and physical process. Similarly, the XPS results also confirmed that the adsorption was mainly a physical process. The superior adsorbing performance of the MHNSs could be attributed to their unique hollow structure and large BET surface area, which provided much active adsorption sites. It is expected that the prepared MHNSs may be a promising adsorbent for water treatment due to its superior adsorbing performance and good stability.

Data Availability

All data included in this study are available upon request by contact with the corresponding author.

Conflicts of Interest

The authors declare that there is no conflict of interest regarding the publication of this paper.

Acknowledgments

This project was financially supported by projects of the China Postdoctoral Science Foundation (No. 2017M610491), Key Program of Natural Science Foundation of Hubei Province (No. 2016CFA079), Scientific Research Plan Project of Education department of Hubei province (No. B2017057), and the Principal Fund of Wuhan Institute of Technology (NO. 2018003).

References

- [1] R. Xu, J. Mao, N. Peng, X. Luo, and C. Chang, "Chitin/clay microspheres with hierarchical architecture for highly efficient removal of organic dyes," *Carbohydrate Polymers*, vol. 188, pp. 143–150, 2018.
- [2] Z. Wen, J. Ke, J. Xu, S. Guo, Y. Zhang, and R. Chen, "One-step facile hydrothermal synthesis of flowerlike Ce/Fe bimetallic oxides for efficient As(V) and Cr(VI) remediation: performance and mechanism," *Chemical Engineering Journal*, vol. 343, pp. 416–426, 2018.

- [3] Z. Wen, Y. Zhang, Y. Wang, L. Li, and R. Chen, "Redox transformation of arsenic by magnetic thin-film MnO_2 nanosheet-coated flowerlike Fe_3O_4 nanocomposites," *Chemical Engineering Journal*, vol. 312, pp. 39–49, 2017.
- [4] Z. Gao, S. Xie, B. Zhang, X. Qiu, and F. Chen, "Ultrathin Mg-Al layered double hydroxide prepared by ionothermal synthesis in a deep eutectic solvent for highly effective boron removal," *Chemical Engineering Journal*, vol. 319, pp. 108–118, 2017.
- [5] S. Luo, F. Qin, Y. Ming, H. Zhao, Y. Liu, and R. Chen, "Fabrication uniform hollow Bi_2S_3 nanospheres via Kirkendall effect for photocatalytic reduction of Cr(VI) in electroplating industry wastewater," *Journal of Hazardous Materials*, vol. 340, pp. 253–262, 2017.
- [6] F. Chen, S. Xie, X. Huang, and X. Qiu, "Ionothermal synthesis of Fe_3O_4 magnetic nanoparticles as efficient heterogeneous Fenton-like catalysts for degradation of organic pollutants with H_2O_2 ," *Journal of Hazardous Materials*, vol. 322, Part A, pp. 152–162, 2017.
- [7] S. Guo, A. Naeem, H. Fida, M. Hamayun, M. Muska, and J. Chen, "Removal of Cu(II) from aqueous solution by iron vanadate: equilibrium and kinetics studies," *Desalination and Water Treatment*, vol. 75, pp. 124–131, 2017.
- [8] S. Guo, Z. Yang, Z. Wen, H. Fida, G. Zhang, and J. Chen, "Reutilization of iron sludge as heterogeneous Fenton catalyst for the degradation of rhodamine B: role of sulfur and mesoporous structure," *Journal of Colloid and Interface Science*, vol. 532, pp. 441–448, 2018.
- [9] J. Ke, X. Li, Q. Zhao, B. Liu, S. Liu, and S. Wang, "Upconversion carbon quantum dots as visible light responsive component for efficient enhancement of photocatalytic performance," *Journal of Colloid and Interface Science*, vol. 496, pp. 425–433, 2017.
- [10] H. Fida, G. Zhang, S. Guo, and A. Naeem, "Heterogeneous Fenton degradation of organic dyes in batch and fixed bed using La-Fe montmorillonite as catalyst," *Journal of Colloid and Interface Science*, vol. 490, pp. 859–868, 2017.
- [11] J.-X. Yu, W. L. Xiong, J. Zhu, J. D. Chen, and R. A. Chi, "Removal of Congo red from aqueous solution by adsorption onto different amine compounds modified sugarcane bagasse," *Clean Technologies and Environmental Policy*, vol. 19, no. 2, article 1243, pp. 517–525, 2017.
- [12] Z. He, J. Yu, Y. Qi, and R. A. Chi, "PMDA-modified biosorbents for enhancement adsorption of basic magenta," *Environmental Earth Sciences*, vol. 70, no. 2, article 2147, pp. 635–642, 2013.
- [13] S. Song, K. Wu, H. Wu, J. Guo, and L. Zhang, "Multi-shelled ZnO decorated with nitrogen and phosphorus co-doped carbon quantum dots: synthesis and enhanced photodegradation activity of methylene blue in aqueous solutions," *RSC Advances*, vol. 9, no. 13, pp. 7362–7374, 2019.
- [14] L. Chen, J. Wei, W. Wang, and C. Wang, "Combination of microalgae cultivation with membrane processes for the treatment of municipal wastewater," *Water Science & Technology*, vol. 68, no. 11, pp. 2374–2381, 2013.
- [15] M. Zhang, L. Wang, T. Zeng et al., "Two pure MOF-photocatalysts readily prepared for the degradation of methylene blue dye under visible light," *Dalton Transactions*, vol. 47, no. 12, pp. 4251–4258, 2018.
- [16] H. Wang, L. Liang, X. Cheng, Y. Luo, and S. Sun, "Facile fabrication of porous ZnS and ZnO films by coaxial electrospinning for highly efficient photodegradation of organic dyes," *Photochemistry and Photobiology*, vol. 94, no. 1, pp. 17–26, 2018.
- [17] J. Huang, Y. Ming, Y. du, Y. Wang, and C. Wang, "Study on the effect of the three-dimensional electrode in degradation of methylene blue by lithium modified rectorite," *Journal of Analytical Methods in Chemistry*, vol. 2016, Article ID 8198235, 6 pages, 2016.
- [18] G. Cheng and F. J. Stadler, "Achieving phase transformation and structure control of crystalline anatase TiO_2 @C hybrids from titanium glycolate precursor and glucose molecules," *Journal of Colloid and Interface Science*, vol. 438, pp. 169–178, 2015.
- [19] Z. Wen, Y. Zhang, S. Guo, and R. Chen, "Facile template-free fabrication of iron manganese bimetal oxides nanospheres with excellent capability for heavy metals removal," *Journal of Colloid and Interface Science*, vol. 486, pp. 211–218, 2017.
- [20] J. Qian, H. Jin, B. Chen et al., "Aqueous manganese dioxide ink for paper-based capacitive energy storage devices," *Angewandte Chemie (International Ed. in English)*, vol. 54, no. 23, pp. 6800–6803, 2015.
- [21] Y. Sun, Z. Fang, C. Wang, K. R. R. M. Ariyawansa, A. Zhou, and H. Duan, "Sandwich-structured nanohybrid paper based on controllable growth of nanostructured MnO_2 on ionic liquid functionalized graphene paper as a flexible supercapacitor electrode," *Nanoscale*, vol. 7, no. 17, pp. 7790–7801, 2015.
- [22] T. Raj Kumar, G. Gnana Kumar, and A. Manthiram, "Biomass-derived 3D carbon aerogel with carbon shell-confined binary metallic nanoparticles in CNTs as an efficient electrocatalyst for microfluidic direct ethylene glycol fuel cells," *Advanced Energy Materials*, vol. 9, no. 16, article 1803238, 2019.
- [23] G. Jenita Rani, M. A. Jothi Rajan, and G. Gnana kumar, "Reduced graphene oxide/ ZnFe_2O_4 nanocomposite as an efficient catalyst for the photocatalytic degradation of methylene blue dye," *Research on Chemical Intermediates*, vol. 43, no. 4, pp. 2669–2690, 2017.
- [24] H.-P. Jing, C.-C. Wang, Y.-W. Zhang, P. Wang, and R. Li, "Photocatalytic degradation of methylene blue in ZIF-8," *RSC Advances*, vol. 4, no. 97, pp. 54454–54462, 2014.
- [25] J. Salamon, Y. Sathishkumar, K. Ramachandran et al., "One-pot synthesis of magnetite nanorods/graphene composites and its catalytic activity toward electrochemical detection of dopamine," *Biosensors and Bioelectronics*, vol. 64, pp. 269–276, 2015.
- [26] G. Gnana Kumar, G. Amala, and S. M. Gowtham, "Recent advancements, key challenges and solutions in non-enzymatic electrochemical glucose sensors based on graphene platforms," *RSC Advances*, vol. 7, no. 59, pp. 36949–36976, 2017.
- [27] M. Ranjani, Y. Sathishkumar, Y. S. Lee, D. Jin Yoo, A. R. Kim, and G. Gnana kumar, "Ni-Co alloy nanostructures anchored on mesoporous silica nanoparticles for non-enzymatic glucose sensor applications," *RSC Advances*, vol. 5, no. 71, pp. 57804–57814, 2015.
- [28] M. Gheju, I. Balcu, and G. Mosoarca, "Removal of Cr(VI) from aqueous solutions by adsorption on MnO_2 ," *Journal of Hazardous Materials*, vol. 310, pp. 270–277, 2016.
- [29] D. Li, X. Wu, and Y. Chen, "Synthesis of hierarchical hollow MnO_2 microspheres and potential application in abatement of VOCs," *Journal of Physical Chemistry C*, vol. 117, no. 21, pp. 11040–11046, 2013.

- [30] Y. Chen, Q. Wang, and T. Wang, "Facile large-scale synthesis of brain-like mesoporous silica nanocomposites via a selective etching process," *Nanoscale*, vol. 7, no. 39, pp. 16442–16450, 2015.
- [31] J. Ke, X. Duan, S. Luo et al., "UV-assisted construction of 3D hierarchical rGO/Bi₂MoO₆ composites for enhanced photocatalytic water oxidation," *Chemical Engineering Journal*, vol. 313, pp. 1447–1453, 2017.
- [32] J. Xiong, G. Cheng, F. Qin, R. Wang, H. Sun, and R. Chen, "Tunable BiOCl hierarchical nanostructures for high-efficient photocatalysis under visible light irradiation," *Chemical Engineering Journal*, vol. 220, pp. 228–236, 2013.
- [33] S. Danwittayakul, M. Jaisai, T. Koottatep, and J. Dutta, "Enhancement of photocatalytic degradation of methyl orange by supported zinc oxide nanorods/zinc stannate (ZnO/ZTO) on porous substrates," *Industrial & Engineering Chemistry Research*, vol. 52, no. 38, pp. 13629–13636, 2013.
- [34] L. Zhang, K. Wu, Y. Zhou et al., "Synthesis of MnO₂@graphene oxide flower-like nanocomposite as adsorbent for methyl orange decolouration," *Micro & Nano Letters*, vol. 12, no. 5, pp. 335–337, 2017.
- [35] M. K. Sahu, S. Mandal, L. S. Yadav, S. S. Dash, and R. K. Patel, "Equilibrium and kinetic studies of Cd(II) ion adsorption from aqueous solution by activated red mud," *Desalination and Water Treatment*, vol. 57, no. 30, pp. 14251–14265, 2015.
- [36] J. Shou and M. Qiu, "Adsorption of copper ions onto activated carbon from capsicum straw," *Desalination and Water Treatment*, vol. 57, no. 1, pp. 353–359, 2014.
- [37] M. Loredó-Cancino, E. Soto-Regalado, R. B. García-Reyes et al., "Adsorption and desorption of phenol onto barley husk-activated carbon in an airlift reactor," *Desalination and Water Treatment*, vol. 57, no. 2, pp. 845–860, 2015.
- [38] T. N. Ramesh, D. V. Kirana, A. Ashwini, and T. R. Manasa, "Calcium hydroxide as low cost adsorbent for the effective removal of indigo carmine dye in water," *Journal of Saudi Chemical Society*, vol. 21, no. 2, pp. 165–171, 2017.
- [39] Y. Xie, C. He, L. Liu et al., "Carbon nanotube based polymer nanocomposites: biomimic preparation and organic dye adsorption applications," *RSC Advances*, vol. 5, no. 100, pp. 82503–82512, 2015.
- [40] H. Faghihian, S. N. Mirsattari, and K. Asghari, "Kinetics & thermodynamics of Cu(II) adsorption by imprinted salen-functionalized silica gel," *Desalination and Water Treatment*, vol. 52, no. 37–39, pp. 7205–7217, 2013.
- [41] P. Koilraj and S. Kannan, "Aqueous fluoride removal using ZnCr layered double hydroxides and their polymeric composites: batch and column studies," *Chemical Engineering Journal*, vol. 234, pp. 406–415, 2013.
- [42] J. Ma, M. Yang, F. Yu, and J. Zheng, "Water-enhanced removal of ciprofloxacin from water by porous graphene hydrogel," *Scientific Reports*, vol. 5, no. 1, article 13578, 2015.
- [43] B. Cheknane, F. Zermane, M. Baudu, O. Bouras, and J. P. Basly, "Sorption of basic dyes onto granulated pillared clays: thermodynamic and kinetic studies," *Journal of Colloid and Interface Science*, vol. 381, no. 1, pp. 158–163, 2012.
- [44] F. Ayari, E. Srasra, and M. Trabelsi-Ayadi, "Low-cost adsorbents for a dye uptake from contaminated water modeling of adsorption isotherms: the Langmuir, Freundlich and Elovich models," *Surface Engineering and Applied Electrochemistry*, vol. 44, no. 6, pp. 489–498, 2008.
- [45] B. Kwakye-Awuah, E. Von-Kiti, I. Nkrumah, R. Erdoó Ikyreve, I. Radecka, and C. Williams, "Parametric, equilibrium, and kinetic study of the removal of salt ions from Ghanaian seawater by adsorption onto zeolite X," *Desalination and Water Treatment*, vol. 57, no. 45, pp. 21654–21663, 2016.
- [46] B. Satilmis and T. Uyar, "Amine modified electrospun PIM-1 ultrafine fibers for an efficient removal of methyl orange from an aqueous system," *Applied Surface Science*, vol. 453, pp. 220–229, 2018.
- [47] S. Chen, Y. Huang, X. Han et al., "Simultaneous and efficient removal of Cr(VI) and methyl orange on LDHs decorated porous carbons," *Chemical Engineering Journal*, vol. 352, pp. 306–315, 2018.
- [48] N. I. Blaisi, M. Zubair, Ihsanullah et al., "Date palm ash-MgAl-layered double hydroxide composite: sustainable adsorbent for effective removal of dyes and eriochrome black-T from aqueous phase," *Environmental Science and Pollution Research*, vol. 25, no. 34, pp. 34319–34331, 2018.
- [49] Y.-z. Ma, D.-f. Zheng, Z.-y. Mo, R.-j. Dong, and X.-q. Qiu, "Magnetic lignin-based carbon nanoparticles and the adsorption for removal of methyl orange," *Colloids and Surfaces A: Physicochemical and Engineering Aspects*, vol. 559, pp. 226–234, 2018.
- [50] K. Rathinam, S. P. Singh, C. J. Arnusch, and R. Kasher, "An environmentally-friendly chitosan-lysozyme biocomposite for the effective removal of dyes and heavy metals from aqueous solutions," *Carbohydrate Polymers*, vol. 199, pp. 506–515, 2018.
- [51] Y. Liu, Y. Tian, C. Luo, G. Cui, and S. Yan, "One-pot preparation of a MnO₂-graphene-carbon nanotube hybrid material for the removal of methyl orange from aqueous solutions," *New Journal of Chemistry*, vol. 39, no. 7, pp. 5484–5492, 2015.
- [52] M. Bhowmik, A. Debnath, and B. Saha, "Fabrication of mixed phase calcium ferrite and zirconia nanocomposite for abatement of methyl orange dye from aqua matrix: optimization of process parameters," *Applied Organometallic Chemistry*, vol. 32, no. 12, article e4607, 2018.
- [53] Y. Gao, S. Q. Deng, X. Jin, S. L. Cai, S. R. Zheng, and W. G. Zhang, "The construction of amorphous metal-organic cage-based solid for rapid dye adsorption and time-dependent dye separation from water," *Chemical Engineering Journal*, vol. 357, pp. 129–139, 2019.
- [54] B. Chen, S. Chen, H. Zhao, Y. Liu, F. Long, and X. Pan, "A versatile β -cyclodextrin and polyethyleneimine bi-functionalized magnetic nanoadsorbent for simultaneous capture of methyl orange and Pb(II) from complex wastewater," *Chemosphere*, vol. 216, pp. 605–616, 2019.
- [55] I. I. Fafous, E. S. Radwan, and J. N. Dawoud, "Kinetics, equilibrium and thermodynamics of the sorption of tetrabromobisphenol A on multiwalled carbon nanotubes," *Applied Surface Science*, vol. 256, no. 23, pp. 7246–7252, 2010.
- [56] R. Niwas, U. Gupta, A. A. Khan, and K. G. Varshney, "The adsorption of phosphamidon on the surface of styrene supported zirconium (IV) tungstophosphate: a thermodynamic study," *Colloids and Surfaces A: Physicochemical and Engineering Aspects*, vol. 164, no. 2–3, pp. 115–119, 2000.
- [57] Y. Yu, Y.-Y. Zhuang, Z.-H. Wang, and M.-Q. Qiu, "Adsorption of water-soluble dyes onto modified resin," *Chemosphere*, vol. 54, no. 3, pp. 425–430, 2004.
- [58] Y. Liu and Y.-J. Liu, "Biosorption isotherms, kinetics and thermodynamics," *Separation and Purification Technology*, vol. 61, no. 3, pp. 229–242, 2008.

- [59] G. Gnana kumar, Z. Awan, K. Suk Nahm, and J. Stanley Xavier, "Nanotubular MnO₂/graphene oxide composites for the application of open air-breathing cathode microbial fuel cells," *Biosensors and Bioelectronics*, vol. 53, pp. 528–534, 2014.
- [60] M. Hu, K. S. Hui, and K. N. Hui, "Role of graphene in MnO₂/graphene composite for catalytic ozonation of gaseous toluene," *Chemical Engineering Journal*, vol. 254, pp. 237–244, 2014.
- [61] J. Ma, F. Yu, L. Zhou et al., "Enhanced adsorptive removal of methyl orange and methylene blue from aqueous solution by alkali-activated multiwalled carbon nanotubes," *ACS Applied Materials & Interfaces*, vol. 4, no. 11, pp. 5749–5760, 2012.
- [62] Ş. S. Bayazit, "Magnetic multi-wall carbon nanotubes for methyl orange removal from aqueous solutions: equilibrium, kinetic and thermodynamic studies," *Separation Science and Technology*, vol. 49, no. 9, pp. 1389–1400, 2014.
- [63] K. Luo, S.-X. Zhao, Y.-F. Wang, S.-J. Zhao, and X.-H. Zhang, "Synthesis of petal-like δ-MnO₂ and its catalytic ozonation performance," *New Journal of Chemistry*, vol. 42, no. 9, pp. 6770–6777, 2018.
- [64] H. Liu, Z. Hu, Y. Su, H. Ruan, R. Hu, and L. Zhang, "MnO₂nanorods/3D-rGO composite as high performance anode materials for Li-ion batteries," *Applied Surface Science*, vol. 392, pp. 777–784, 2017.

